

Morphology Engineering of Porous Media for Enhanced Solar Fuel and Power Production

Silvan Suter & Sophia Haussener

JOM

The Journal of The Minerals, Metals &
Materials Society (TMS)

ISSN 1047-4838

JOM

DOI 10.1007/s11837-013-0787-9



Your article is published under the Creative Commons Attribution license which allows users to read, copy, distribute and make derivative works, as long as the author of the original work is cited. You may self-archive this article on your own website, an institutional repository or funder's repository and make it publicly available immediately.

Morphology Engineering of Porous Media for Enhanced Solar Fuel and Power Production

SILVAN SUTER¹ and SOPHIA HAUSSENER^{1,2}

1.—Institute of Mechanical Engineering, École Polytechnique Fédérale de Lausanne, 1015 Lausanne, Switzerland. 2.—e-mail: sophia.haussener@epfl.ch

The favorable and adjustable transport properties of porous media make them suitable components in reactors used for solar energy conversion and storage processes. The directed engineering of the porous media's morphology can significantly improve the performance of these reactors. We used a multiscale approach to characterize the changes in performance of exemplary solar fuel processing and solar power production reactors incorporating porous media as multifunctional components. The method applied uses imaging-based direct numerical simulations and digital image processing in combination with volume averaging theory to characterize the transport in porous media. Two samples with varying morphology (fibrous vs. foam) and varying size range (mm vs. μm scale), each with porosity between 0.46 and 0.84, were characterized. The obtained effective transport properties were used in continuum-scale models to quantify the performance of reactors incorporating multifunctional porous media for solar fuel processing by photoelectrochemical water splitting or power production by solar thermal processes.

INTRODUCTION

The direct conversion of solar energy into a storable, high-energy density fuel via solar thermochemistry or photoelectrochemistry and the solar production of power via solar thermal processes are promising renewable fuel processing and power production routes. The essential requirements for the processes' impact on our fuel and power economy are their sustainable, efficient, stable, and economic implementation via solar reactors and their assembly into practical large-scale systems.^{1–4} The engineering of solar reactors needs to address various issues including optimal design and operational conditions for enhanced coupled multiphysics transport and the integration and optimization of multiscale components, e.g., porous media. The latter is of special interest as porous media exhibit favorable and tunable transport properties. Particularly interesting is the observed fourfold increase in efficiency of a solar reactor for the thermochemical splitting of water and CO_2 into synthesis gas when changing the porous absorber and reactant morphology from a sintered backed bed to a highly porous foam morphology.^{5,6} Similar influences on performance are expected for solar receivers used for thermal power production,

which rely on porous absorber and heat exchangers of various morphologies,^{7,8} or for photoelectrochemical fuel production devices relying on microstructured to nanostructured photoelectrodes^{9–13} or separators.¹⁴

The systematic understanding of how the transport properties of porous media change for distinct base morphologies (foam or fibrous structure) but varying morphological characteristics, i.e., varying porosity, is of practical interest due to the straightforward synthesis of such porous media. Systematic direct numerical studies on how morphology and its tailoring can influence the transport properties have been conducted for micron-sized sintered packed beds,¹⁵ reticulate porous ceramics and packed beds,^{16,17} and foams.¹⁸

We used a multiscale approach to quantify the changes in the performance of solar reactors incorporating porous media with varying morphologies (foams and fibers) and morphological properties (characteristic size and porosity). This multiscale approach consisted of (1) the transport quantification in porous structures by applying tomography-based approaches that incorporate the exact morphology into pore-scale numerical simulations^{19–22} in combination with image processing techniques,¹⁸ and (2) the subsequent use of the transport characteristics in continuum-scale models of reactors

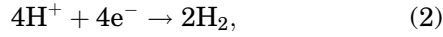
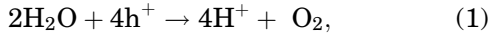
processing fuel via photoelectrochemical processes or power via solar thermal processes.

METHODOLOGY

Multiscale Approach

Continuum-Scale Models of Reactors Incorporating Multifunctional Porous Media

Photoelectrochemistry is a promising direct solar-to-fuel processing route. It uses the photon energy to generate electron–hole pairs in a semiconductor absorber. The electron–hole pairs are separated via an electric field and used at liquid–solid interfaces to drive catalyzed electrochemical reactions such as water electrolysis described by



in an acidic environment. Ions are transported through an ion-conducting phase to conserve the charge. This is schematically shown in Fig. 1a for a solar electrochemical reactor incorporating a multifunctional porous slab.

Solar thermal processes for renewable power production use the solar energy as sensible heat to heat a (pressurized) heat transfer fluid, which is used in subsequent power cycles.⁸ This is schematically shown in Fig. 1b for a solar receiver incorporating a multifunctional porous slab.

Radiative Heat Transfer The radiative transport in porous media, composed of a transparent and an opaque phase, was given by the volume-averaged radiative transfer equation²³

$$\mathbf{s} \cdot \nabla I = -\beta_e I + \alpha_e I_b + \frac{\sigma_{\text{scat},e}}{4\pi} \int_0^{4\pi} \Phi_{\text{scat},e} I d\Omega \quad (3)$$

β_e , $\sigma_{\text{scat},e}$, and $\Phi_{\text{scat},e}$ were the effective extinction and scattering coefficients, and scattering phase function, to be determined by direct numerical simulations. Collimated solar irradiation with 1.5 AM spectral distribution was irradiating the boundary at the top of the slab. The lateral walls were assumed perfectly specular; the inlet and outlet ambient boundaries were black surrounding at 0 K. The reflected R and the transmitted T fraction of the incident radiation were calculated by integrating the fluxes over the inlet and outlet boundary. The absorbed radiation, $A = 1 - R - T$, contributed to the divergence of the radiative flux. We used a path-length-based Monte Carlo method for solving the volume-averaged radiative transfer equations.²⁴

Photoelectrochemical Fuel Processing The solar-to-fuel efficiency of a photoelectrochemical fuel processing reactor incorporating multifunctional porous medium.²⁵

$$\eta = \frac{iE_0}{Q_{\text{sol},\text{in}}} \frac{i - nFD_{\text{H}_2,e}c_{\text{sat}}/t}{i} \quad (4)$$

was calculated using equivalent circuit models.^{26,27} i represented the superficial current density of the cell, which was calculated as the intersection between the load curve of the cell,

$$\Phi = E_0 + \eta_a + |\eta_c| + i \frac{t}{\kappa_e} + i \frac{t}{\sigma_e} \quad (5)$$

and the power curve of the dual absorber material,

$$i = i_{\text{ph}} - i_0 \left(\exp\left(\frac{q\Phi}{kT}\right) - 1 \right) \quad (6)$$

The parameters in Eq. 6 were calculated for the absorbed fraction of the irradiation (Eq. 3) using the Shockley-Queisser limit²⁸ for a dual-absorber tandem

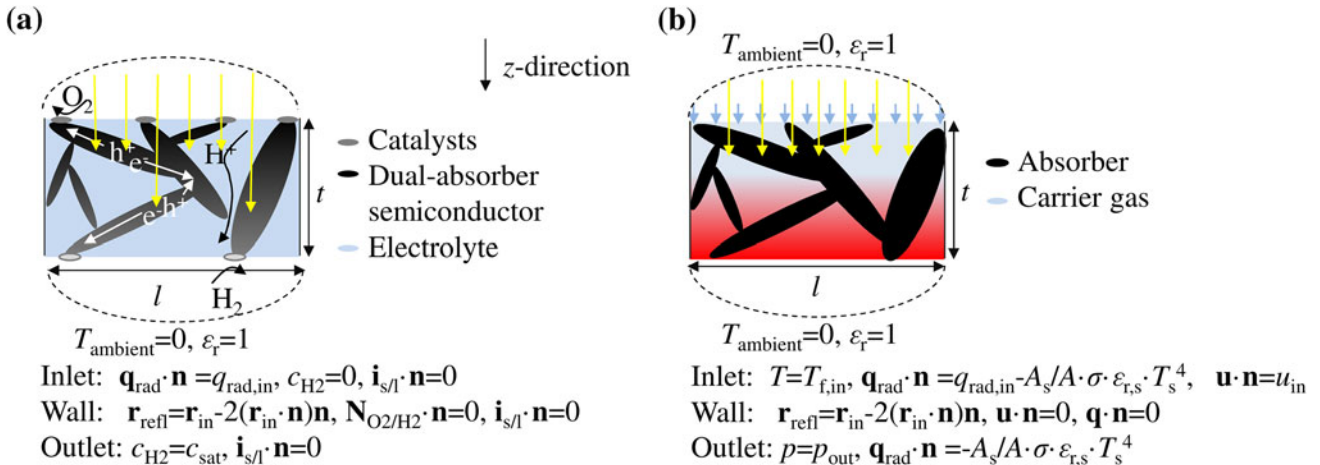


Fig. 1. Schematics of the 1-D slabs of multifunctional porous media to be used for solar (a) electrochemical fuel and (b) thermal power processing, and the corresponding boundary conditions for the continuum-scale models.

porous medium. This approach neglected possible bulk and surface recombination mechanism in the absorber. The effective ionic and electronic conductivities, κ_e and σ_e , were calculated via the direct numerical simulation technique, and the reaction overpotentials at the anode and cathode, η_a and η_c , were approximated by Tafel expressions assuming that reaction occurred at the top and bottom solid phase boundary. The second fraction on the right side of Eq. 4 described the fraction of the current density that was not lost due to product crossover via diffusion through the membrane. The effective hydrogen diffusivity was calculated via direct numerical simulations and the worst-case scenario for crossover was assumed, i.e., the hydrogen evolution side completely saturated with hydrogen and the oxygen evolution side completely hydrogen starved.¹⁴

Solar Thermal Power Production We used a quasi-one-dimensional (1-D) model to solve the steady-state mass, momentum, and energy conservation equations at local thermal nonequilibrium in the solar thermal power production reactor incorporating a multifunctional porous media. The volume-averaged energy conservation equations were given by

$$0 = \nabla \cdot (k_{e,s} \nabla T_s) - h_{sf} A_0 (T_s - T_f) + q_r \quad (7)$$

$$\rho c_p \nabla \cdot (\mathbf{u} T_f) = \nabla \cdot (k_{e,f} \nabla T_f) + h_{sf} A_0 T_f (T_s - T_f) \quad (8)$$

where the temperature variables represented intrinsic averages. It was assumed that only the solid fraction of the inlet and outlet boundary (A_s) reradiated, describing the boundary condition for the inlet and outlet boundaries

$$Q_{\text{rerad}} = (1 - r) A_s \sigma T_s^4 \quad (9)$$

where r was the directional-hemispherical reflectivity of the material. The lateral walls were symmetric boundaries. The carrier gas was modeled as an ideal gas with temperature-dependent properties. The solar-to-power efficiency of the slab of multifunctional porous medium was described by

$$\eta = \frac{\dot{m} (h_{\text{outlet}} - h_{\text{intlet}})}{Q_{\text{sol,in}} + W_{\text{pump}}} \eta_{\text{Carnot}, T_f|_{z=t}} \quad (10)$$

The pumping work was given by the volume-averaged momentum conservation²⁹

$$W_{\text{pump}} = \Delta p u_f A = \left(\frac{\mu_f}{K} u_f + \rho_f F u_f^2 \right) t u_f A \quad (11)$$

with u_f the superficial velocity average. The effective transport properties permeability K and the Forchheimer coefficient F were determined via the direct numerical simulations. An inlet mass flow and an outlet pressure were set at the corresponding boundaries.

Pore-Scale Transport Characterization

Radiative Heat Transfer β_e , $\sigma_{\text{scat},e}$, and $\Phi_{\text{scat},e}$ were calculated by solving the pore-scale radiative heat transfer equations. Radiative distribution functions were used to determine the effective radiative properties³⁰ using a collision-based Monte Carlo technique. An opaque solid phase and a transparent fluid phase were assumed. The laws of geometrical optics were applicable as $\pi d/\lambda \gg 1$.

Conductive Heat Transfer $k_{e,s}$ and $k_{e,f}$ were calculated by solving the steady-state conduction equations within the void and solid phases^{20,22,31,32} in a representative cubical sample of porous medium applying predefined inlet and outlet temperatures, insulating lateral wall boundaries, and providing continuity in temperature and heat flux at the solid–fluid phase boundary. For the orthotropic fibrous sample, the temperature boundary conditions were applied along the z -direction. $k_{e,s}$ and $k_{e,f}$ were determined as the asymptotic cases where the heat conductivity of the fluid phase was significantly smaller than the heat conductivity of solid phase ($k_f \ll k_s$) and vice versa ($k_s \ll k_f$).

Convective Heat Transfer The Nu correlations were calculated by solving the heat, mass, and momentum (incompressible and laminar) conservation equations within the fluid phase of the porous media for an isothermal solid phase. The fluid phase of cubical porous samples within a square duct with inlet and outlet regions was used as computational domain.^{21,22,31,32} Uniform inlet velocity and temperature, constant outlet pressure, symmetry at the lateral duct walls, and no-slip and constant temperature at the solid–fluid interface were assumed. Inlet velocities in the range of 0.0008–0.5 m/s (corresponding to $d_{\text{void,foam}}$ -based Re between 0.1 and 100) and Pr numbers of 0.5, 1, and 10 were simulated. For the orthotropic fibrous sample, the inlet and outlet boundaries were applied along the z -direction.

Mass Transfer K and F were determined by using the previously calculated pressure and velocity vector fields.²² For the orthotropic fibrous sample, the pressure boundary conditions were applied along the z -direction. $D_{\text{H}_2,e}$ was calculated by^{33,34}

$$D_{\text{H}_2,e} = D_{\text{H}_2} \frac{\varepsilon}{\tau_{\text{mean}}^2} \quad (12)$$

The mean tortuosity, $\tau_{\text{mean}} = l_{\text{path,mean}}/t$, was numerically determined using the previously calculated velocity vector field and determining the lengths of 3600 streamlines with uniformly distributed starting points at the medium inlet for Re = 0.1.²²

Charge transfer κ_e and σ_e were calculated by solving the charge transport equations, i.e., Ohm's law, in the ionic and electronic phases. The methodology

was analogous to the methodology used for the determination of the effective thermal conductivity in porous media.^{20,22} Again, the asymptotic cases were considered, i.e., κ_e at $\kappa_s \ll \kappa_f$ and σ_e at $\sigma_f \ll \sigma_s$, respectively. For the orthotropic fibrous sample, the potential boundary conditions were applied along the z -direction.

Morphology

Exemplary, we used two distinct morphologies with continuous, percolating solid phases: (1) foam-like structures and (2) fibrous-like structures. The foam-like samples have been manufactured by a template method using a ceria-based slurry and 10 ppi polyurethane sponges.⁶ The fibrous samples were ceria felts manufactured by Zircar Zirconia, Inc. (Florida, NY, USA). These structures were imaged via x-ray computed tomography. The initial samples can be subjected to fabrication variations, e.g., increasing strut and fiber sizes by additional applications of slurry or coating. This variation in the fabrication process and the corresponding changes in the sample's morphology were virtually reproduced by digital image processing, i.e., dilation operations with spherical structuring elements.

The three-dimensional (3-D) rendering of the two base morphologies and varying porosities, i.e., increasing numbers of applied coating steps, i.e., dilation operations with increasing size of the structural element, are depicted in Fig. 2. The z -direction described one of the two symmetry axis of the orthotropic fibrous sample, perpendicular to the fiber alignment.

The characteristic sizes of the two original samples differed by two orders of magnitude. To allow for a direct comparison and a meaningful size range for the photoelectrochemical application, the foam-like sample was shrunk by a factor of 100 to represent a third type of media exhibiting the same

morphology as the original foam but in the same size range as the fibrous material. We thus investigated two foam-like samples with two distinctly different size ranges (foam original and foam shrunk) and one fiber sample.

The mean pore diameters, represented as the largest spherical pore within the pore space, were calculated via opening operations and were $d_{\text{void,foam,o}} = 2.6, 2.3, 2.0,$ and 1.7 mm for the original foam-like samples for decreasing porosity. The shrunk foam-like sample's pore diameters were $d_{\text{void,foam,s}} = 26, 23, 20,$ and 17 μm for decreasing porosity. The mean fiber and pore diameter were calculated via digital image processing, i.e., connectivity calculations, and they were $d_{\text{solid,fiber}} = 24, 36, 48,$ and 59 μm and $d_{\text{void,fiber}} = 95, 83, 71,$ and 59 μm for decreasing porosity, respectively. The specific surface areas were calculated via two-point correlations and fitted to a second-order polynomial functions

$$A_0 = -117740\varepsilon^2 + 147250\varepsilon - 1116 \quad (13)$$

$$A_0 = (-2277\varepsilon^2 + 2533\varepsilon + 262) \frac{d_{\text{void}}}{d_{\text{void,o}}} \quad (14)$$

for fibrous and foam-like (original and shrunken) samples, respectively. The anisotropy of the samples was characterized via mean intercept lengths³⁵ and showed a degree of anisotropy of 0.23 and 0.55 for the foam and the fibrous samples, respectively.

RESULTS

Transport Characterization

Normalized β_e of the foam (original and shrunken) and fibrous samples with different porosities is depicted in Fig. 3. The increase in β_e with decreasing

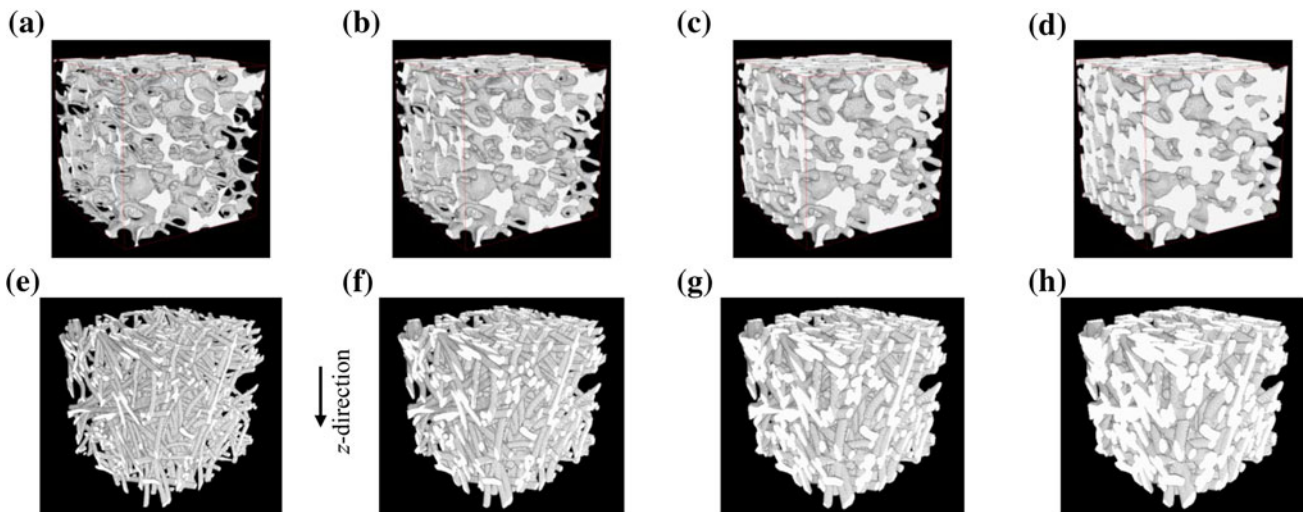


Fig. 2. Foam-like morphology with sample edge length = 20 mm (a–d),¹⁸ fibrous morphology with sample edge length = 0.49 mm (e–h), for porosities 0.84 (a, f), 0.72 (b, f), 0.59 (c, g), and 0.46 (d, h).

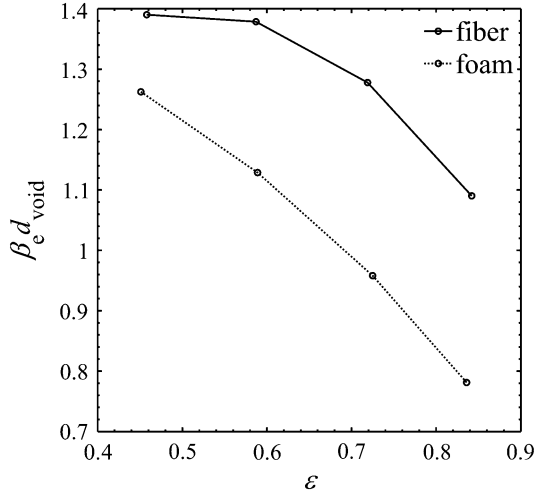


Fig. 3. Normalized effective extinction coefficient as a function of the sample porosity for original and shrunken foam-like samples (dotted line), and fibrous samples (solid line).

porosity was linear and is in accordance with the decreasing characteristic pore size for decreasing porosity. The increase in $\beta_e/\beta_{e,\varepsilon=0.84}$ with decreasing porosity was more pronounced for the foam sample.

$\Phi_{\text{scat},e}$ for diffusely reflecting phase boundaries showed little dependence on the morphology and porosity and were fitted to a second-order polynomial

$$\Phi_{\text{scat},e} = 0.58\mu_{\text{scat}}^2 - 1.40\mu_{\text{scat}} + 0.81 \quad (15)$$

$$\Phi_{\text{scat},e} = 0.59\mu_{\text{scat}}^2 - 1.41\mu_{\text{scat}} + 0.80 \quad (16)$$

for fibrous and foam-like (original and shrunken) samples, respectively.

The Nusselt numbers were given by

$$\text{Nu} = 5.54 + (0.71\varepsilon^2 - 0.63\varepsilon + 0.30)\text{Re}^{\sqrt{1.70-1.39\varepsilon}}\text{Pr}^{0.6} \quad (17)$$

$$\text{Nu} = 6.55 + (1.35\varepsilon^2 - 1.29\varepsilon + 0.62)\text{Re}^{\sqrt{0.93-0.55\varepsilon}}\text{Pr}^{0.6} \quad (18)$$

for fibrous and foam-like (original and shrunken) samples, respectively. The foam-like samples showed an almost constant Nu at low Re, independent of porosity, while for $\text{Re} > 10$, the Nu was highly porosity dependent.¹⁸ The Nu numbers of the fibrous sample showed almost no porosity dependence for the whole Re range investigated.

The normalized effective conductivities are depicted in Fig. 4. The effective thermal and ionic conductivities of the fluid phase of the fiber and foam-like samples were similar, i.e., $\kappa_{e,\text{foam}}/\kappa_{e,\text{fib}} = k_{e,f,\text{foam}}/k_{e,f,\text{fib}} = 0.95\text{--}1.05$. σ_e/σ_s and $k_{e,s}/k_s$ of the fibers were significantly lower than for the foam-like samples, i.e., $\sigma_{e,\text{foam}}/\sigma_{e,\text{fib}} = k_{e,s,\text{foam}}/k_{e,s,\text{fib}} = 2\text{--}25$, with the largest

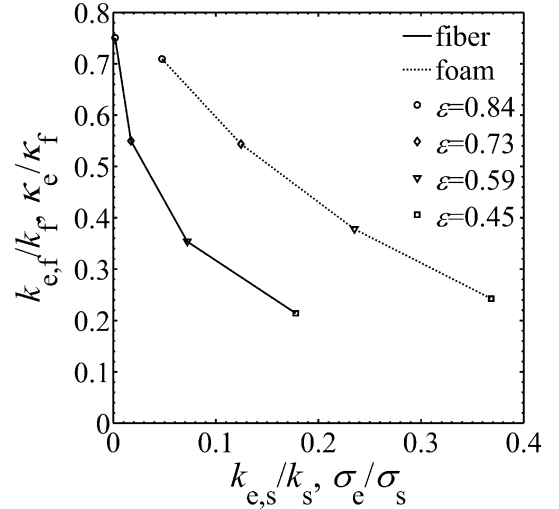


Fig. 4. Normalized effective thermal and ionic conductivity of the fluid phase as a function of the normalized thermal or electrical conductivity of the solid phase for fibrous (solid line) and original and shrunken foam-like (dotted) samples for varying porosities.

differences for high porosities. The decreased effective electronic and thermal conductivities of the solid phase of the fibrous samples were explained by the more perpendicular arrangement of the fibers to the electrical potential and heat flux, respectively.

The normalized K and F of the fibrous and foam-like samples for various porosities are depicted in Fig. 5. K of the original foam samples was three orders of magnitude larger than K of the fibrous samples. F differs by almost two orders of magnitude. The samples' permeabilities can be accurately (RMS = 2%) described by exponential functions in porosity ($K = a\exp(b\varepsilon)$), i.e., lumping all the other morphological characteristics into two constants.

τ_{mean} of the fiber and foam-like samples is given in Table I. $\tau_{\text{mean},\text{fiber}} > \tau_{\text{mean},\text{foam}}$ especially at lower porosities as dead ends and recirculation zones were more frequent. Consequently, the effective (hydrogen) diffusivity of the foam-like samples was larger than the effective diffusivity of the fibrous sample at similar porosities.

Application to Solar Fuel Processing and Solar Thermal Power Generation

The pure porosity-dependent absorption behavior of the fibrous and foam-like samples (original and shrunken) with $r = 0.1$ is depicted in Fig. 6. The foam-like samples with largest porosity reached maximal absorptance ($T < 0.005$) within $t/d_{\text{void},\text{foam}} \geq 7$, while the fibrous samples required $t/d_{\text{void},\text{fiber}} \geq 5$. The maximal absorption achievable was only dependent on the sample porosity and not the sample morphology ($(A_{\text{fiber}} - A_{\text{foam}})/A_{\text{fiber}} \leq 0.3\%$). The fibrous and the shrunken foam samples achieved the maximal achievable A within a sample thickness of only a few hundred microns; the original foam sample required thicknesses larger than 20 cm.

Photoelectrochemical Fuel Processing

We used Pt and RuO₂ catalysts for the hydrogen and oxygen evolution reactions with $i_{0,a} = 10^{-8}$ A/cm², $i_{0,c} = 10^{-3}$ A/cm², $A_a = 35$ mV/dec, and $A_c = 30$ mV/dec.³⁶ The area of the porous slab modeled was 25 cm². The solar irradiation was

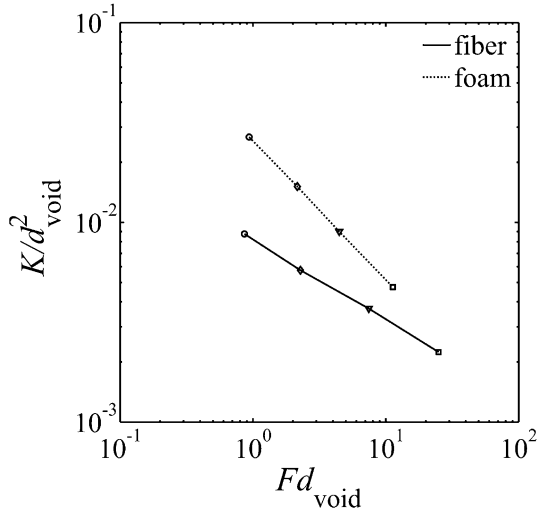


Fig. 5. Permeability and Forchheimer coefficient for fibrous (solid line) and original and shrunken foam-like (dotted, dashed) samples for varying porosities.

Table I. Mean tortuosity for the fiber and original and shrunken foam-like samples for various porosities

ε	0.84	0.72	0.59	0.46
$\tau_{\text{mean,fiber}}$	1.269	1.394	1.550	1.746
$\tau_{\text{mean,foam}}$	1.150	1.234	1.342	1.482

1 kW/m², collimated and 1.5 AM. The energy band gaps of the dual absorber were 1.6 eV and 1.0 eV, corresponding to a current matching absorber combination.²⁵ The ambient temperature was assumed ($T = 300$ K) and the hydrogen saturation concentration in water was 0.78 mol/m³. We used $\kappa_1 = 40$ S/m, which corresponds to the ionic conductivity of 1 M sulfuric acid. σ_s varied significantly depending on the materials and their doping; we assumed $\sigma_s = 1$ S/m.

The efficiency of the multifunctional porous slab used for photoelectrochemical fuel production using the two different base morphologies (fiber and shrunken foam) and four different porosities is given in Fig. 7. The initial gain in efficiency resulted from the increase in absorbed solar radiation. The decrease in efficiency for larger thicknesses was a result of the dominance of the ohmic losses, especially the losses due to conduction in the solid absorber phase. The decrease in efficiency was observed at smaller sample thicknesses for the fibrous samples than the shrunken foam samples as $\sigma_{e,\text{fiber}} < \sigma_{e,\text{foam,s}}$. For samples with larger porosities, the thickness at which the ohmic losses started to dominate did not yet allow for complete radiation absorption, and consequently, the observed maximal efficiency was significantly lower than the maximal achievable efficiency for maximal absorption. The absorption-limited efficiency was only reached for the fibers with $\varepsilon = 0.46$ and the shrunken foam samples with $\varepsilon = 0.46$ –0.719.

Solar Thermal Power Production A sample of area 0.503 m² was irradiated by a collimated solar flux of 1000 kW/m². Air was the heat transfer fluid assumed, modeled as an ideal gas with temperature-dependent properties³⁷ and inlet mass flow of $\dot{m} = 0.4$ kg/s, initial temperature of 298 K, and an absolute pressure of 10 bars. These boundary conditions were an estimate of a 1 MW pressurized air

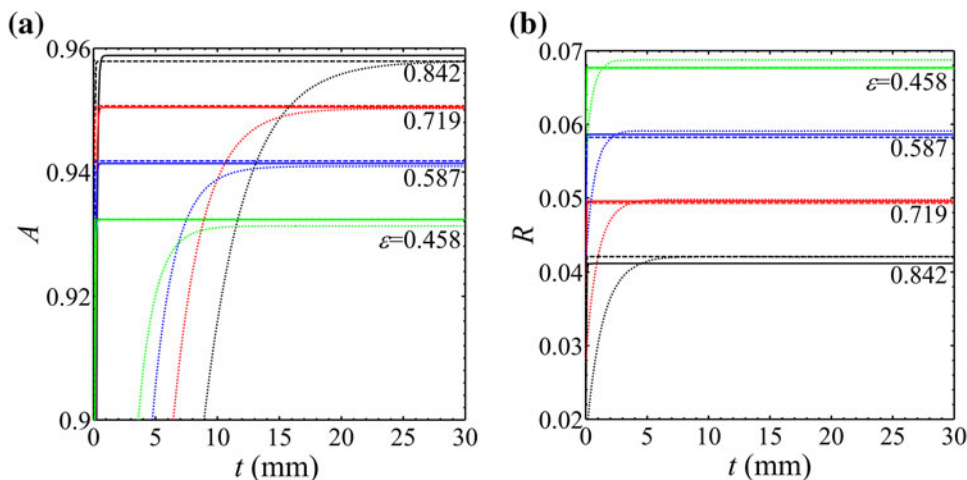


Fig. 6. (a) Absorptance and (b) reflectance as a function of layer thickness for fibrous (solid lines), original (dotted lines), and shrunken (dashed lines) foam-like samples with $r = 0.1$ and varying porosity.

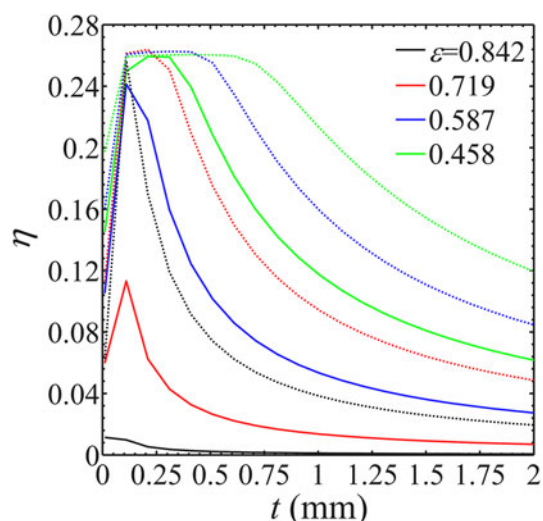


Fig. 7. Solar-to-fuel efficiency of a multifunctional porous slab for photoelectrochemical solar fuel processing. The efficiency is shown as a function of layer thickness for fibrous (solid lines) and shrunk foam-like (dashed lines) samples with varying porosity.

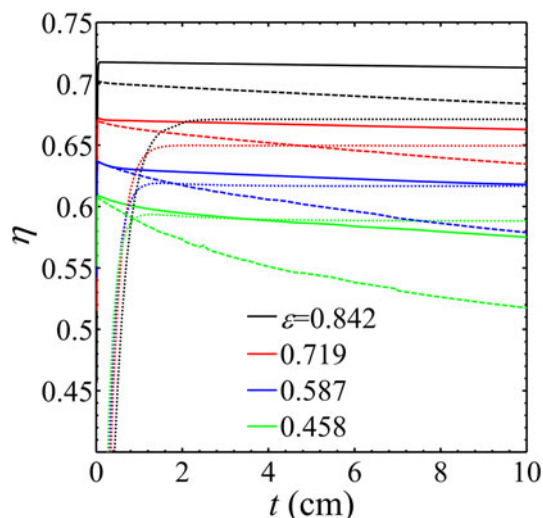


Fig. 8. Overall efficiency of a multifunctional porous slab for solar thermal power production. The efficiency is shown as a function of layer thickness for fibrous (solid lines), original (dotted lines), and shrunk (dashed lines) foam-like samples with varying porosity.

receiver for solar-driven gas turbines.⁸ Sintered silicon carbide was used as the solid absorber with $r = 0.1$.³⁷ The efficiency of the multifunctional 1-D slab used for solar thermal power production for the three different morphologies and four different porosities is given in Fig. 8. The fibrous samples reached the maximal absorptance for slab thicknesses of several hundred microns, and the highest efficiency was achieved for samples with highest porosities as their reflectance were the smallest. The shrunken foam-like samples reached their maximum efficiencies within the first 100 μm due to the larger extinction coefficients; however, a higher reflectance for low porosity led to slightly lower maximum values. Increasing the sample thickness led to a decrease in efficiency because the pressure losses through the slab became significant. The influence of the pump work onto the efficiency of the fibrous samples was less significant but still apparent. In contrast, the original foam-like samples showed no decrease in efficiency with increasing thickness. The original foam samples at comparable porosity required larger sample thicknesses to reach the maximal efficiency due to significantly lower extinction coefficients. The maximum efficiency of a fibrous sample and the shrunken foam-like samples was always larger compared to the original foam-like sample with the same porosity mainly due to their larger specific surface area and enhanced convective heat transfer.

CONCLUSIONS

A multiscale experimental–numerical methodology has been used to quantify the gain in performance due to engineering of the morphology of

porous media used as absorber, heat exchanger, charge conductor, and reaction site in solar reactors. Two base morphologies have been investigated, i.e., fibrous and foam-like samples. Their exact morphologies were experimentally obtained via x-ray computed tomography and subsequently manipulated by digital image processing to vary characteristic morphological sizes and porosity, both at a constant base morphology. The obtained morphologies (fibrous, original, and shrunken foam samples) were used in direct numerical simulations for the determination of their effective heat, mass, and charge transport properties, which were used in continuum-scale models of reactors incorporating 1-D multifunctional porous slabs performing photoelectrochemical hydrogen generation and solar thermal power production.

We showed that heat, mass, and charge transport in porous media cannot accurately be described based on only two morphological characteristics, e.g., porosity and a characteristic length. For the particular cases of fibrous, original foam, and shrunken foam-base morphologies, we determined the porosity-dependent effective extinction coefficients, effective scattering phase functions, permeabilities and Forchheimer coefficients, effective diffusivities and tortuosity distributions, Nu correlations, and effective ionic, electronic, and thermal conductivities.

The developed continuum-scale models of reactors incorporating 1-D slabs of porous media used in a photoelectrochemical hydrogen generation process and a solar thermal power production process were used to quantify the influence of morphology on process performance. We observed that the morphology leading to optimized efficiencies was

dependent on the application of the porous media. The efficiency of photoelectrochemical fuel processing could be increased by a factor of 23 when using a shrunken foam morphology instead of a fibrous morphology at high porosities. The efficiency of solar thermal power production increased by a factor of 1.2 and the required slab thickness was reduced by a factor of 12 when using a highly porous fibrous sample with fiber diameters in the μm range instead of a low porosity foam sample with pore diameters of a few mm. The study showed—in the limit of the validity of the continuum model’s assumptions—that the morphology, scale, and porosity of the multifunctional porous components incorporated in solar reactors significantly influence their performances.

ACKNOWLEDGEMENTS

We acknowledge Jan Marti from ETH Zurich performing initial studies on transport in fibrous materials at the Professorship of Renewable Energy Carriers and Prof. Steinfeld heading this Professorship.

OPEN ACCESS

This article is distributed under the terms of the Creative Commons Attribution License which permits any use, distribution, and reproduction in any medium, provided the original author(s) and the source are credited.

REFERENCES

1. S. Chu and A. Majumdar, *Nature* 488, 294 (2012).
2. N. Lewis and D. Nocera, *Proc. Natl. Acad. Sci.* 103, 15729 (2006).
3. J. Newman, P.G. Hoertz, C.A. Bonino, and J.A. Trainham, *J. Electrochem. Soc.* 159, A1722 (2012).
4. J.A. Turner, *Science* 285, 687 (1999).
5. P. Furler, J.R. Scheffe, and A. Steinfeld, *Energy Environ. Sci.* 5, 6098 (2012).
6. P. Furler, J. Scheffe, M. Gorbar, L. Moes, U. Vogt, and A. Steinfeld, *Energy Fuels* 26, 7051 (2012).
7. M. Röger, L. Amsbeck, B. Gobereit, and R. Buck, *J. Sol. Energy Eng.* 133, 031009 (2011).
8. I. Hischer, P. Leumann, and A. Steinfeld, *J. Sol. Energy Eng.* 134, 021003 (2012).
9. M. Graetzel, *Curr. Opin. Colloid Interf. Sci.* 4, 314 (1999).
10. A. Kay, I. Cesar, and M. Grätzel, *J. Am. Chem. Soc.* 128, 15714 (2006).
11. R. van de Krol, Y. Liang, and J. Schoonman, *J. Mater. Chem.* 18, 2311 (2008).
12. K. Sivula, F. Le Formal, and M. Grätzel, *Chem. Mater.* 21, 2862 (2009).
13. C. Liu, J. Tang, H.M. Chen, B. Liu, and P. Yang, *Nano Lett.* 13, 2989 (2013).
14. S. Haussener, C. Xiang, J.M. Spurgeon, S. Ardo, N.S. Lewis, and A.Z. Weber, *Energy Environ. Sci.* 5, 9922 (2012).
15. S. Haussener and A. Steinfeld, *Materials* 5, 192 (2012).
16. A. Akolkar and J. Petrasch, *Int. J. Heat Mass Trans.* 54, 4775 (2011).
17. A. Akolkar and J. Petrasch, *Transport Porous Media*, 1 (2012).
18. S. Suter, A. Steinfeld, and S. Haussener, *Int. J. Heat Mass Trans.* (submitted).
19. J. Petrasch, P. Wyss, and A. Steinfeld, *J. Quant. Spectrosc. Radiat. Trans.* 105, 180 (2007).
20. J. Petrasch, B. Schrader, P. Wyss, and A. Steinfeld, *J. Heat Trans.* 130, 032602 (2008).
21. J. Petrasch, F. Meier, H. Friess, and A. Steinfeld, *Int. J. Heat Fluid Flow* 29, 315 (2008).
22. S. Haussener, P. Coray, W. Lipinski, P. Wyss, and A. Steinfeld, *J. Heat Trans.* 132, 023305 (2010).
23. W. Lipinski, J. Petrasch, and S. Haussener, *J. Quant. Spectrosc. Radiat. Trans.* 111, 253 (2010).
24. J. Petrasch, S. Haussener, and W. Lipinski, *J. Quant. Spectrosc. Radiat. Trans.* 112, 1450 (2011).
25. S. Haussener, S. Hu, C. Xiang, A.Z. Weber, and N. Lewis, *Energy Environ. Sci.* (2013). doi:10.1039/C3EE41302K.
26. R.E. Rocheleau and E.L. Miller, *Int. J. Hydrogen Energy* 22, 771 (1997).
27. S. Hu, C. Xiang, S. Haussener, A.D. Berger, and N.S. Lewis, *Energy Environ. Sci.* 6, 2984 (2013).
28. W. Shockley and H.J. Queisser, *J. Appl. Phys.* 32, 510 (1961).
29. S. Whitaker, *The Method of Volume Averaging, Theory and Applications of Transport in Porous Media* (Dordrecht, the Netherlands: Kluwer Academic Publisher, 1999).
30. M. Tancrez and J. Taine, *Int. J. Heat Mass Transf.* 47, 373 (2004).
31. H. Friess, S. Haussener, A. Steinfeld, and J. Petrasch, *Int. J. Numer. Methods Eng.* 93, 1040 (2013).
32. Ansys Inc., *Ansys 14* (Canonsburg, PA: ANSYS, Inc., 2013).
33. W. Ullman and R. Aller, *Limnol Oceanogr.* 27, 552–556 (1982).
34. J. Van Brakel and P. Heertjes, *Int. J. Heat Mass Trans.* 17, 1093 (1974).
35. I. Arganda-Carreras, F.P. Cordelieres, R.P. Dougherty, J.S. Jackson, B. Schmid, J.R. Hutchinson, M. Doube, M.M. Klosowski, and S.J. Shefelbine, *Bone* 47, 1076 (2010).
36. M.G. Walter, E.L. Warren, J.R. McKone, S.W. Boettcher, Q. Mi, E.A. Santori, and N.S. Lewis, *Chem. Rev.* 110, 6446 (2010).
37. AIChE Design Institute for Physical Properties, *DIPPR Project 801—Full Version* (New York, NY: Design Institute for Physical Property Research/AIChE, 2012).